Local environment analysis of dopants in ceramics by x-ray absorption near-edge structure with the aid of first-principles calculations

2009 J. Phys.: Condens. Matter 21 104211

(http://iopscience.iop.org/0953-8984/21/10/104211)

IOP Publishing Journal of Physics: Condensed Matter

J. Phys.: Condens. Matter **21** (2009) 104211 (8pp) doi:10.1088/0953-8984/21/10/104211

Local environment analysis of dopants in ceramics by x-ray absorption near-edge structure with the aid of first-principles calculations

Tomoyuki Yamamoto[1,3], Yoshitada Kawashima[1], Yasuyuki Kusakabe[1], Shigeru Matsuda[1], Yutaka Mizuoka[1], Yuki Nakade[1] and Toshihiro Okajima[2]

[1] Faculty of Science and Engineering, Waseda University, Shinjuku, Tokyo 169-8555, Japan
[2] Kyusyu Synchrotron Radiation Research Center, Tosu, Saga 841-0005, Japan

E-mail: tymmt@waseda.jp

Received 18 September 2008, in final form 3 November 2008
Published 10 February 2009
Online at stacks.iop.org/JPhysCM/21/104211

Abstract
Three types of functional ceramic materials, (1) dilute magnetic semiconductor, (2) phosphor and (3) electrolyte of a solid fuel cell, are fabricated by the conventional solid state reaction method. Local environments of dopants in these ceramic materials here synthesized are systematically investigated by using the x-ray absorption near-edge structure (XANES) with the aid of first-principles calculations. Our present analytical method by combined use of XANES and first principles calculations has successfully explained the local environment of dopants in the above ceramic materials.

1. Introduction

It is well known that the doping technique is widely used to give additional properties, e.g. electronic, magnetic and optical properties, especially in semiconducting materials. In order to understand the mechanism of appearance of new properties by doping and to design new materials with desired properties by the doping technique, it is essential to know the local environment of dopants on an atomic scale. There are some analytical methods to investigate the local environment of dopants. Among these methods, x-ray absorption near-edge structure (XANES) is one of the most powerful methods, which enables us to determine the local environment of dopant at an ultra-dilute concentration level [1]. Conventional analysis of XANES is based on a fingerprint type method, in which the experimental XANES spectrum of interest is compared with the experimental spectra of reference materials. However, it is difficult to determine the local environment of dopant by such an experimental fingerprint type analysis. To overcome this difficulty, a lot of attempts to reproduce the experimental XANES profiles by theoretical calculations have been made. If quantitative agreement can be obtained between experimental and calculated XANES spectra, we can get the theoretical fingerprints. For these theoretical XANES calculations, various kinds of calculating methods, i.e. the molecular orbital method, band-structure method and multiple scattering method [2], were employed. However, the theoretical spectra do not always reproduce the experimental spectra satisfactorily. There are several factors contributing to the poor agreement. One of the most typical reasons is improper treatment of the interaction between a core hole and an excited electron, i.e. the core-hole effect. Proper inclusion of the core-hole effect is mandatory for reproducing experimental spectra by theoretical calculations. Recently, quantitative reproductions of experimental XANES from many different kinds of crystals have been reported [3, 4] by the first-principles band-structure calculations within the density functional theory (DFT) using the orthogonalized linear combination of atomic orbitals (OLCAO) method [5] and the full-potential augmented plane wave plus local orbitals (APW + lo) method [6]. In these calculations, the core hole was directly included in the self-consistent calculations. Interaction among core holes was minimized using supercells. Thereby the core-hole

[3] Address for correspondence: Waseda University, 3-4-1 Okubo Shinjuku-ku, Tokyo 169-8555, Japan.

effect was included within the framework of the one-electron approximation.

In the present paper, we have summarized the local environment analysis of dopants in three kinds of functional ceramic materials, i.e. (1) dilute magnetic semiconductor (Mn- and Fe-codoped In_2O_3), (2) phosphor (Pr-doped $SrTiO_3$ and $CaTiO_3$, Pr- and Ga-codoped $SrTiO_3$) and (3) electrolyte of a solid fuel cell (Y-doped CeO_2), by XANES analysis with the aid of first-principles calculations. For these target subjects denoted above by (1)–(3), Mn K and Fe K, Pr L_3 and Ga K, and Y L_3 XANES were investigated here, respectively.

2. Experimental and computational procedures

All the samples were prepared by the conventional solid state reaction method. Prior to the XANES measurements, all the samples were characterized by using the x-ray diffraction (XRD) technique to check whether the synthesized material was single phase or not. All the present sample powders were determined to be a single phase by XRD measurements. Two types of XANES measurements, i.e. hard and soft x-ray XANES measurements, were carried out. The former XANES spectra, i.e. hard x-ray XANES, were collected at the beamlines in two synchrotron facilities, i.e. BL01B1 in SPring8 and BL15 in Kyusyu Synchrotron Radiation Center, in the transmission mode. Synchrotron radiation from the storage rings was monochromatized by the Si(111) or Si(311) double-crystal monochromators. The latter, soft x-ray, XANES measurements, only Y L_3 XANES in the present paper, were carried out at BL-1A in UVSOR by the total electron yield method, in which an InSb(111) double-crystal monochromator was employed. The sample powders were mounted on carbon adhesive tape, and were settled on the first dynode of the electron multiplier.

First-principles calculations were carried out to obtain the theoretical XANES spectra by using the full-potential augmented plane wave plus local orbital (APW + lo) package (WIEN2k [6]). As is well established, the introduction of the core-hole effect is mandatory to reproduce the spectral fine structure of XANES [3]. In the present study, the core-hole effect is introduced by removing one core electron of interest and putting one additional electron at the bottom of the conduction band, which approximately corresponds to the final state of the x-ray absorption process of interest. The muffin-tin radius of each atom was chosen as large as possible in the cell, and $R_{MT}K_{max}$, which corresponds to the plane wave cutoff, was set by using the product of the smallest R_{MT} and K_{max} (3.0–3.5 $Ryd^{1/2}$). The Monkhorst–Pack scheme [7] was employed for k-point sampling in the reciprocal space, in which VN is set to be larger than 10 000, where V and N are the volume of the cell and the number of k-points, respectively. Here the supercell was used to minimize the interaction between core holes due to the three dimensional periodic boundary condition in our band-structure calculations. Transition energy is calculated by a difference of total electronic energies between initial (ground) and final (core-hole) states. Spectral profiles were calculated by the product of projected partial density of state for the electric dipole allowed transition of interest and the radial part of the transition probability.

3. Results and discussion

3.1. Dilute magnetic semiconductor

Semiconductors doped with dilute magnetic elements, which are called dilute magnetic semiconductors (DMSs), have been extensively studied since the discovery of carrier-induced ferromagnetism in $In_{1-x}Mn_xAs$ and $Ga_{1-x}Mn_xAs$ [8, 9]. After these discoveries, many attempts to increase the Curie temperature were made, which yielded room temperature ferromagnetism in DMSs. Most of this research on DMSs has been limited to using thin films, but recently it was reported that the dilute magnetic semiconducting ceramic In_2O_3:(Mn, Fe) showed room temperature ferromagnetism [10]. Then the local environment of the magnetic elements, i.e. Mn and Fe ions, in In_2O_3 was examined. The sample specimen, $(In_{0.94}Mn_{0.03}Fe_{0.03})_2O_3$, was fabricated by using commercially available high purity powders of In_2O_3, $MnCO_3$ and Fe_2O_3. After these powders were mixed and ground in an agate mortar, they were pressed into a pellet form and sintered in air for 12 h at 1423 K. Prior to the XANES measurements, the magnetic property of this specimen was examined by a superconducting quantum interference device (SQUID) and a vibrating sample magnetometer (VSM), as shown in figures 1(a) and (b). From the results of these experiments, the room temperature

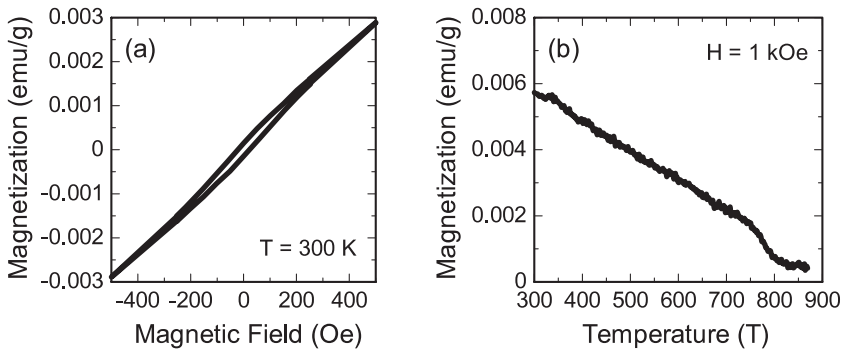

Figure 1. (a) Magnetization versus magnetic field curve of In_2O_3:(Mn, Fe) at 300 K using a SQUID and (b) temperature dependence of magnetization at 1 kOe using a VSM.

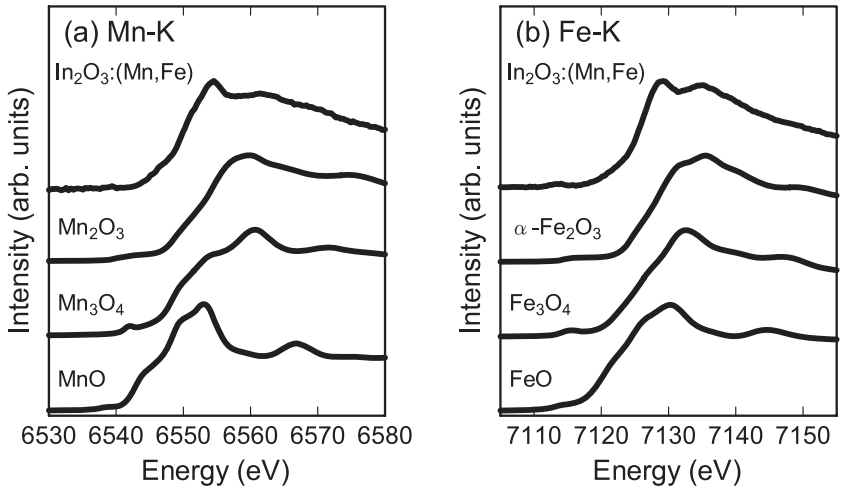

Figure 2. Observed (a) Mn K and (b) Fe K XANES spectra of In_2O_3:(Mn, Fe) and reference oxide materials.

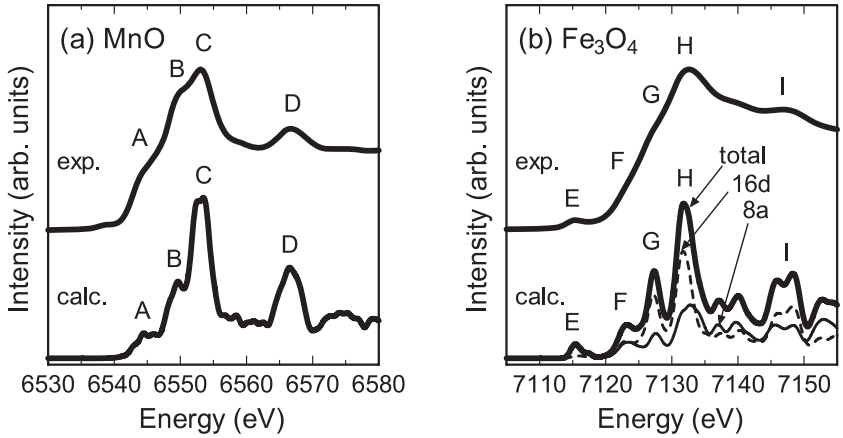

Figure 3. Comparison of XANES spectra of (a) Mn K of MnO and (b) Fe K of Fe_3O_4 between experiments and calculations. Thin solid and dashed lines denote calculated spectra from Fe at 16d and 8a sites, respectively, and the thick solid line is the sum of these two in (b). Calculated transition energies are corrected by (a) $\Delta E_{\mathrm{Mn}} = -19.5$ eV and (b) $\Delta E_{\mathrm{Fe}} = -20.0$ eV.

ferromagnetism in this specimen was confirmed and the Curie temperature was estimated at around 800 K. Observed Mn K and Fe K XANES spectra of In_2O_3:(Mn, Fe) are shown in figures 2(a) and (b) together with the reference Mn and Fe oxides, respectively. Both of the spectral profiles of In_2O_3:(Mn, Fe) show different features from those of the reference oxide materials, which indicates that the local environments of Mn and Fe ions are different from those of these reference oxides. From the results of XRD and these comparisons of XANES spectra, it is suggested that both the Mn and Fe ions are substituted in In_2O_3. In order to confirm this suggestion, first-principles calculations were performed to obtain the theoretical XANES spectra. First, XANES spectra of the reference Mn and Fe oxides were calculated to check the accuracy of the calculations. Here MnO and Fe_3O_4 were chosen for calculation. Cell sizes of the present calculations are a $2 \times 2 \times 2$ supercell of conventional rock-salt structured MnO (64 atoms) and a unit cell of spinel structured Fe_3O_4 (56 atoms). Spin polarized calculations were carried out for both cases. Resultant theoretical XANES spectra of MnO and Fe_3O_4 are compared with the experimental ones in figures 3(a) and (b), respectively. Characteristic features of the experimental Mn K and Fe K XANES spectra are well reproduced by the present calculations, when the transition energy is corrected by $\Delta E_{\mathrm{Mn}} = -19.5$ eV ($\Delta E/E = 0.003$) and $\Delta E_{\mathrm{Fe}} = -20.0$ eV ($\Delta E_{\mathrm{Fe}}/E = 0.003$) for Mn and Fe K edges, respectively. Then the Mn and Fe substituted models in In_2O_3 were separately calculated, in which one of the In ions is replaced by Mn or Fe ions in the unit cell of the bixbyite structured In_2O_3 consisting of 80 atoms. Resulting theoretical Mn K and Fe K XANES spectra of Mn- and Fe-doped In_2O_3 are shown in figures 4(a) and (b), respectively. As shown in this figure, characteristic features in observed XANES spectra of In_2O_3:(Mn, Fe) are well reproduced by the present models and the calculated spectral profiles are clearly distinguishable from the calculated ones for reference oxide materials. It is noted that the transition energy is also well reproduced by the present calculations, if the same values of the energy shifts as for the reference oxides, i.e. ΔE_{Mn} and ΔE_{Fe}, are given. From these results, it can be concluded that Mn and Fe ions are substituted at the In site in the present specimen, $(In_{0.96}Mn_{0.03}Fe_{0.03})_2O_3$.

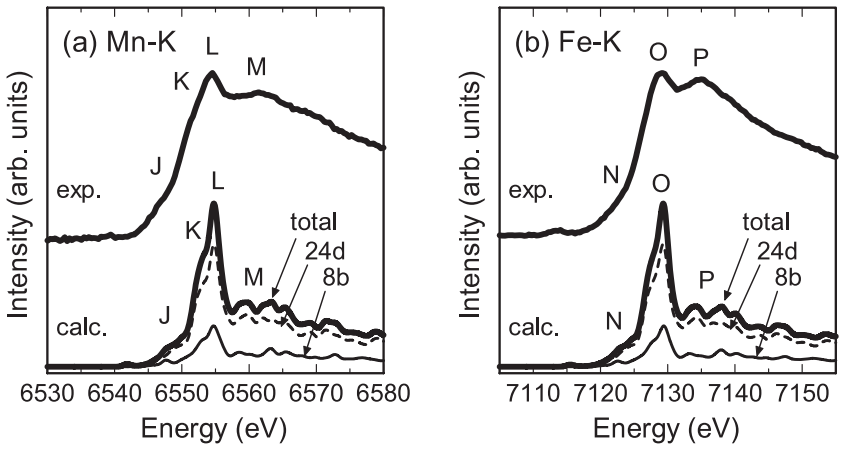

Figure 4. Comparison of XANES spectra of (a) Mn K and (b) Fe K of In_2O_3:(Mn, Fe) between experiments and calculations. Thin solid and dashed lines denote calculated spectra from Mn or Fe at 24d and 8b sites, respectively, and thick solid lines are the sums of these two. Calculated transition energies are corrected by (a) $\Delta E_{\mathrm{Mn}} = -19.5$ eV and (b) $\Delta E_{\mathrm{Fe}} = -20.0$ eV.

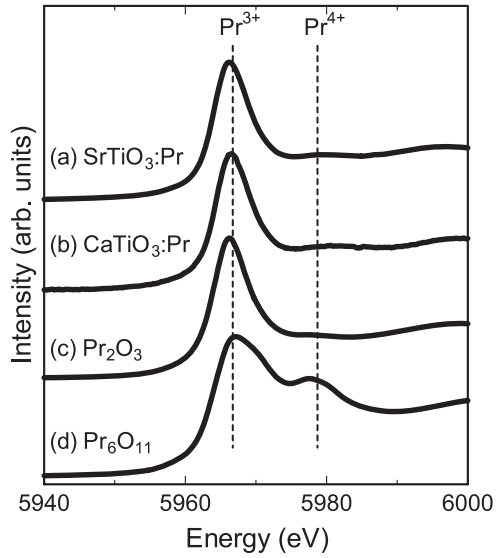

Figure 5. Observed Pr L_3 XANES spectra of Pr-doped (a) $SrTiO_3$ and (b) $CaTiO_3$ and the reference Pr oxides ((c) Pr_2O_3 and (d) Pr_6O_{11}).

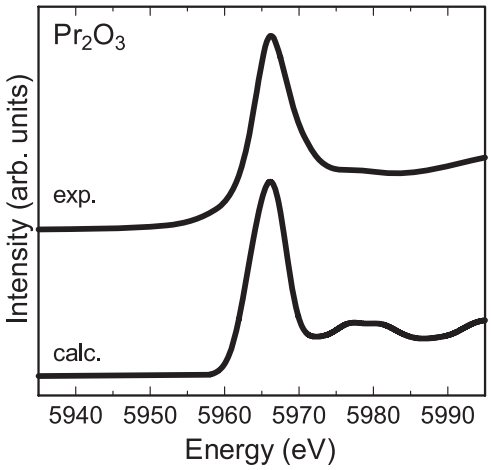

Figure 6. Comparison of Pr L_3 XANES spectra of Pr_2O_3 between experiment and calculation.

3.2. Phosphor materials

Rare-earth-doped oxide materials with the perovskite type of structure have been extensively studied because of their applications in phosphor. Here Pr-doped $SrTiO_3$ and $CaTiO_3$, which are known as red light emitting phosphors [11], have been chosen and the charge state of doped Pr ions in $SrTiO_3$ and $CaTiO_3$, which plays a key role to understand the luminescence property, was examined by chemical shift in XANES spectra. Commercially available high purity powders of $SrCO_3$, $CaCO_3$, TiO_2 and Pr_2O_3 with a cation ratio, i.e. (Sr + Ti):Pr and (Ca + Ti):Pr, of 1.99:0.01 were mixed and ground in an agate mortar, and were calcined in air for 2 h at 1423 K. Resulting powders were mixed and ground again, and were pressed into a pellet form. Finally, these pellets were sintered in air for 6 h at 1523 K. In order to determine the charge state of Pr ions in $SrTiO_3$ and $CaTiO_3$, Pr L_3 XANES spectra were observed, and are shown in figure 5 together with those of reference oxide materials, i.e. Pr_2O_3 and Pr_6O_{11}. In Pr_2O_3 and Pr_6O_{11}, charge states of Pr ions are Pr^{3+} and $Pr^{3+} + Pr^{4+}$ with a ratio of Pr^{3+}:Pr^{4+} = 1:2, respectively. As shown in figure 5, only one intense peak is observed in the Pr L_3 XANES of Pr_2O_3, which originates from Pr^{3+}, while two peaks from Pr^{3+} and Pr^{4+} are seen in that of Pr_6O_{11}. By comparing the peak energies of XANES spectra of Pr-doped $SrTiO_3$ and $CaTiO_3$ with those of the reference spectra, charge states of Pr ions in $SrTiO_3$ and $CaTiO_3$ can be determined experimentally, which shows that Pr ions are Pr^{3+} in these two perovskite type oxides. We also performed first-principles calculations for Pr-doped $SrTiO_3$ and $CaTiO_3$. Prior to the calculations of Pr-doped $SrTiO_3$ and $CaTiO_3$, Pr L_3 XANES of reference Pr oxide, i.e. Pr_2O_3, was examined. In this calculation, a 2 × 2 × 2 supercell (40 atoms) of the hexagonal structured unit cell of Pr_2O_3 was employed. The calculated Pr L_3 XANES spectrum of Pr_2O_3 is compared with the experimental one in figure 6. Although the experimental

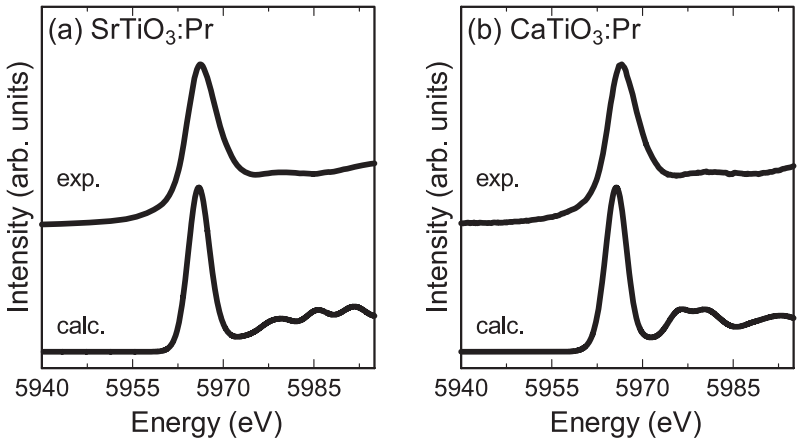

Figure 7. Comparison of Pr L_3 XANES spectra of Pr-doped (a) $SrTiO_3$ and (b) $CaTiO_3$ between experiments and calculations.

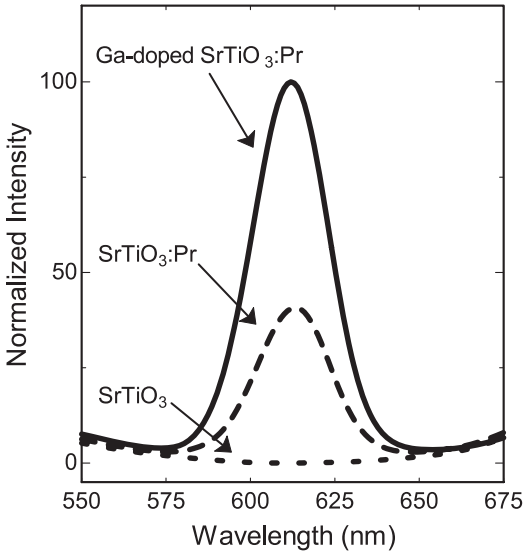

Figure 8. Photoluminescence spectra of Ga-doped $SrTiO_3$:Pr excited by UV (365 nm).

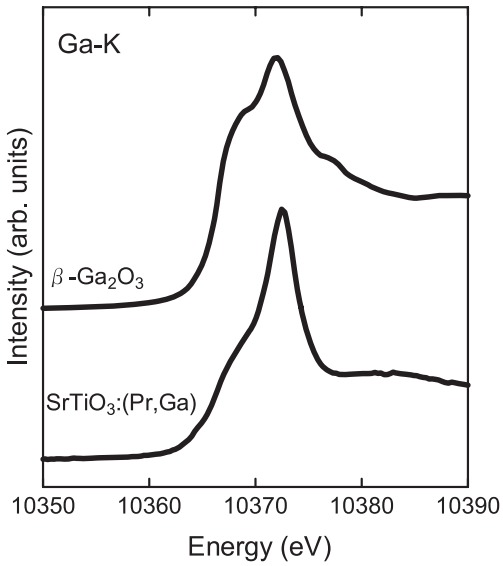

Figure 9. Observed Ga K XANES spectra of Ga-doped $SrTiO_3$ and β-Ga_2O_3.

Pr L_3 XANES spectrum of Pr_2O_3 has only one sharp peak with a satellite shoulder on the higher energy side, the experimental profile is well reproduced by the present calculation, when the transition energy is corrected by -16.0 eV. For the XANES calculations of Pr-doped $CaTiO_3$ and $SrTiO_3$, one Sr^{2+} ion is replaced by a Pr^{3+} ion in a $2 \times 2 \times 2$ supercell (40 atoms) of the cubic perovskite structured unit cell of $SrTiO_3$ and in a $2 \times 2 \times 1$ supercell (80 atoms) of the orthorhombic perovskite structured unit cell of $CaTiO_3$ with a space group of $Pbnm$, respectively. Calculated Pr L_3 XANES spectra of Pr-doped $SrTiO_3$ and $CaTiO_3$ are compared with experimental ones in figures 7(a) and (b), respectively. Only one intense peak can be seen in the calculated spectra of both Pr-doped $SrTiO_3$ and $CaTiO_3$, which reproduce the experimental ones.

It was also reported that the additional doping of Al and Ga ions in $SrTiO_3$:Pr and $CaTiO_3$:Pr increases the intensity of red light photoluminescence [12, 13]. Here the local environment of additionally doped Ga ions in $SrTiO_3$:Pr is investigated by the Ga K XANES. The sample was prepared by the same procedure as for Pr-doped $SrTiO_3$, in which β-Ga_2O_3 was additionally used for starting material with the Ga concentration of 1.5 at.% to other cations (Sr, Ti and Pr ions), i.e. (Sr + Ti + Pr):Ga = 1.97:0.03. Photoluminescence spectra of $SrTiO_3$, $SrTiO_3$:Pr and Ga-doped $SrTiO_3$:Pr here synthesized are shown in figure 8. As shown in this figure, additional Ga doping into Pr-doped $SrTiO_3$ increases the photoluminescence by a factor of approximately 2.5. Observed Ga K XANES spectra are shown in figure 9 with that of β-Ga_2O_3, and show a clear difference between these two spectral profiles. First, the Ga K XANES spectrum of β-Ga_2O_3 was calculated, which is compared with the experimental one in figure 10. In this calculation, a $1 \times 3 \times 2$ supercell (60 atoms) of the monoclinic unit cell of β-Ga_2O_3 was employed. The calculated Ga K XANES spectrum of β-Ga_2O_3 reproduced the experimental characteristic profiles of the earlier report [14], when the transition energy was corrected by $\Delta E = -41.5$ eV. Two types of substitution models of Ga ions in $SrTiO_3$:Pr were

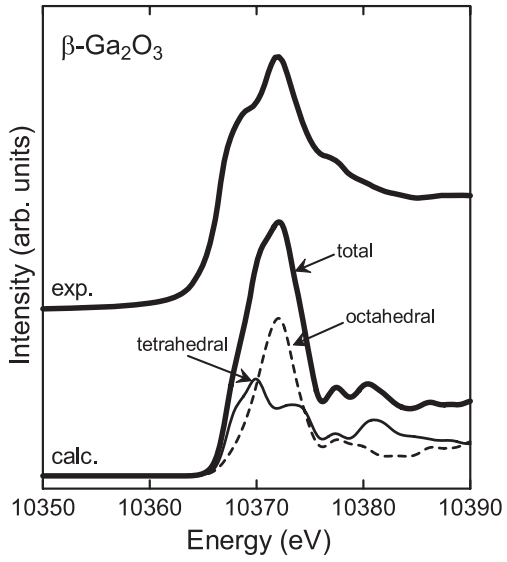

Figure 10. Comparison of Ga K XANES spectra of β-Ga_2O_3 between experiment and calculation.

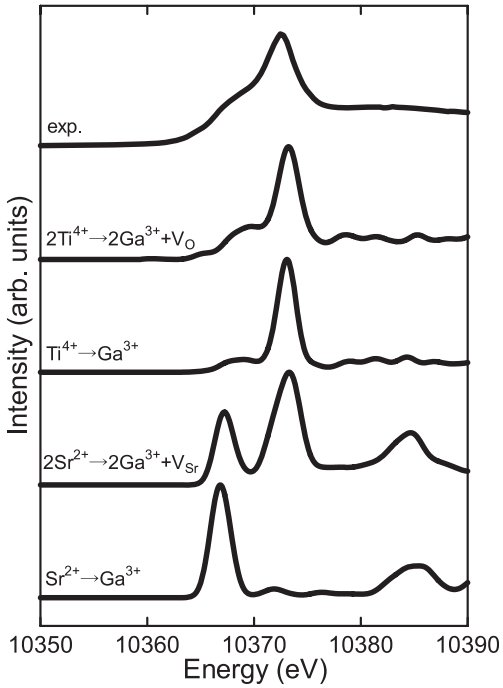

Figure 11. Comparison of Ga K XANES spectra of Ga-doped $SrTiO_3$:Pr between experiment and calculations.

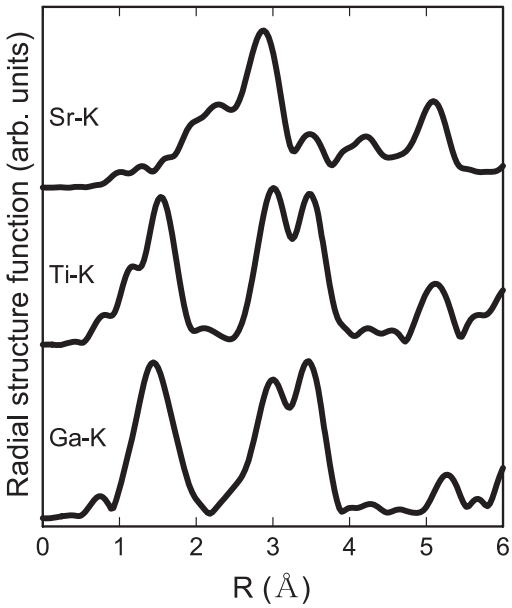

Figure 12. Experimental radial structure functions of Sr and Ti of $SrTiO_3$ and Ga of Ga-doped $SrTiO_3$:Pr from Sr K, Ti K and Ga K EXAFS.

constructed, which are the simple substitution and the vacancy models. In the former model, Sr^{2+} or Ti^{4+} are replaced by Ga^{3+} ions, while two of the Sr^{2+} or Ti^{4+} ions are replaced by two Ga^{3+} ions and one Sr^{2+} (Sr-vacancy model) or one O^{2-} (O-vacancy model) vacancy, respectively, is introduced to compensate the electronic charge of the calculated supercells in the later model. In the Sr-vacancy model the two most distant Sr ions are replaced by two Ga ions and one nearest neighboring Sr ion from one of the substituted Ga ions is removed from the cell, while the nearest Ti ion pair is replaced by a pair of Ga ions and the O ion between these two is removed in the O-vacancy model[4]. Calculated Ga K XANES spectra of these substituted models are compared with the experimental one in figure 11. A significant difference between these calculated spectra appears, in which the calculated XANES spectrum of the O-vacancy model shows a better comparison with the observed one than those of other models. This means the Ga ions are likely to substitute at the Ti site associated with the oxygen vacancy in $SrTiO_3$. Another type of analysis by extended x-ray absorption fine structure (EXAFS) was also carried out. Experimental radial structure functions of Sr and Ti of $SrTiO_3$ and Ga of Ga-doped $SrTiO_3$:Pr deduced from Sr K, Ti K and Ga K EXAFS spectra are shown in figure 12. The resultant radial structure function of the Ga ion is similar to that of Ti, but quite different from that of Sr. This result also indicates that the Ga ion must sit on the Ti site, but not on the Sr site. It is sometimes dangerous to determine the local environment of doped ions by only one piece of experimental or theoretical evidence. However, in the present case, all of the results here investigated, i.e. (1) Ga K XANES measurement, (2) theoretical XANES and (3) EXAFS, show that doped Ga ions are likely to substitute at Ti site in $SrTiO_3$.

[4] Several Sr- and O-vacancy models were calculated, changing the configurations of positions of vacancies by the first-principles projector augmented wave package VASP. After geometry optimization with this package, total electronic energies of the calculated models are examined, in which two models, i.e. Sr- and O-vacancy models, described in the main text have the lowest total electronic energies among the calculated models, respectively.

3.3. Electrolyte of solid fuel cell

It was reported that CeO_2 doped with divalent and/or trivalent cations has high oxygen ion conductivity [15]. In order to understand the mechanism of this high oxygen conductivity,

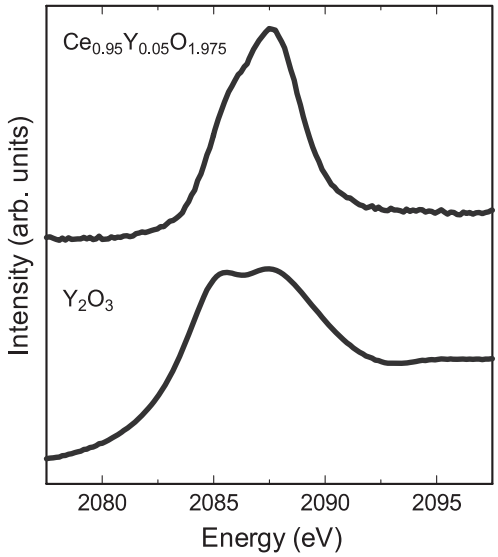

Figure 13. Observed Y L_3 XANES spectra of Y_2O_3 and Y-doped CeO_2.

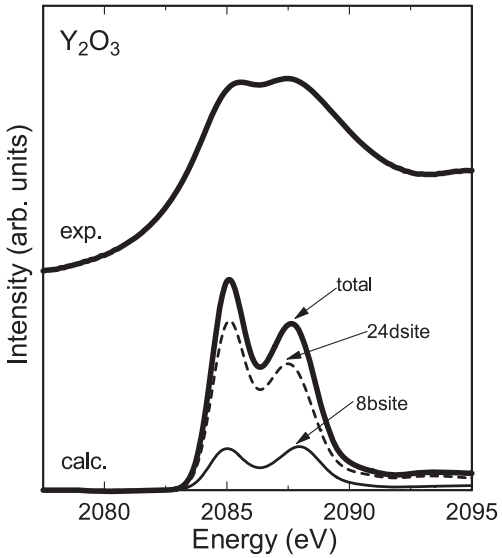

Figure 14. Comparison of Y L_3 XANES spectra of Y_2O_3 between experiment and calculation.

it is essential to understand the vacancy formation mechanism due to the doping of divalent and/or trivalent cations. Here Y-doped CeO_2 is chosen to investigate the vacancy formation mechanism by combined use of Y L_3 XANES and first-principles calculation. The sample specimen was prepared from a mixture of high purity powders of CeO_2 and Y_2O_3 with an atomic molar ratio of Ce:Y = 0.95:0.05, which were calcined at 1523 K for 10 h in air after mixing and grinding, and sintered at 1773 K for 3 h in air. Observed Y L_3 XANES spectra of Y-doped CeO_2 and reference oxide, i.e. Y_2O_3, are shown in figure 13. A clear difference between these observed spectra appears. First, the first-principles XANES spectrum of Y_2O_3 was obtained by using the bixbyite structured unit cell of Y_2O_3 (80 atoms) to calibrate the theoretical transition energy, which is compared with the experimental one in figure 14.

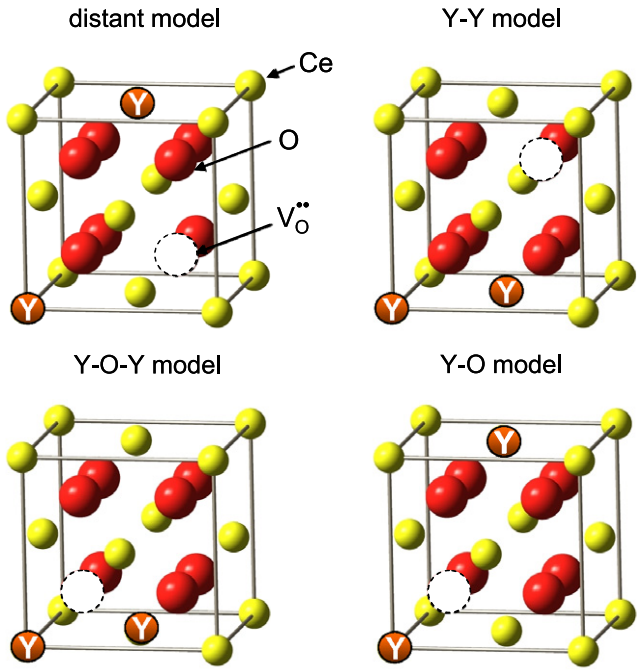

Figure 15. Illustration of calculated models of Y-doped CeO_2. (This figure is in colour only in the electronic version)

The characteristic feature is well reproduced by the present calculation with the energy correction of −12.4 eV. Next the Y L_3 XANES spectrum of Y-doped CeO_2 was investigated by using the four types of representative vacancy models, which are shown in figure 15. Since it is widely accepted that an oxygen vacancy is introduced when Y ions are doped in CeO_2, it is assumed here that the substitution, $2Y^{3+} \leftrightarrow 2Ce^{4+} + O^{2-}$, occurs to control a charge balance in the cell. In the first and second models, two nearest neighboring Ce ions are replaced by two Y ions and an oxygen vacancy is created between these two substituted Y ions (Y–O–Y model), and at distant position from these two Y ions (Y–Y model), respectively. In the third and fourth models, two distant Ce ions are replaced by two Y ions and the oxygen vacancy is placed at the first nearest neighboring site from one of the substituted Y ions (Y–O model), and at a distant site from both of the substituted Y ions (distant model), respectively. Calculated Y L_3 XANES spectra of these four vacancy models with different configurations of substituted Y ions and oxygen vacancy are compared with the experimental one for Y-doped CeO_2 in figure 16. The spectral width becomes broader when the oxygen vacancy is located at the first nearest neighboring site from the doped Y ions, i.e. in Y–O and Y–O–Y models, which yields the disagreement with the experimental XANES profile. Both the calculated spectra of Y–Y and distant models reproduced the experimental one. It is noted that a significant difference could not be seen when the oxygen vacancy is away from the Y ions, which means that Y L_3 XANES is not so sensitive to determine the second nearest ion (first nearest cation) in the present case. From this comparison, it can be concluded that the oxygen vacancy is likely to be away from the substituted Y ions.

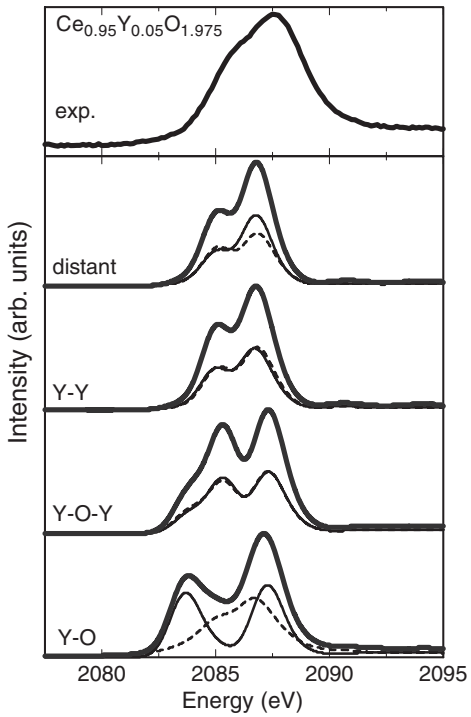

Figure 16. Comparison of Y L_3 XANES spectra of Y-doped CeO_2 between experiment and calculations.

4. Conclusion

Local environment analysis of dopants in three kinds of ceramic materials, i.e. (1) dilute magnetic semiconductor, (2) phosphor and (3) electrolyte of a fuel cell, has been carried out on an atomic scale by the XANES measurements with the aid of the first-principles calculations. Observed XANES spectra have been quantitatively well reproduced by our present first-principles calculations. This type of analytical method for dopants in newly developed functional materials is very useful to understand the mechanism of their properties. In addition, it should be emphasized that there is no limitation, in principle, to apply this method to any other types of materials.

Acknowledgments

This work was partially supported by the Waseda University Grant for Special Research Projects. The synchrotron radiation experiments at SPring-8 were performed with the approval of the Japan Synchrotron Radiation Research Institute (JASRI) (proposal No 2008A1274).

References

[1] Tanaka I, Mizoguchi T, Matsui M, Yoshioka S, Adachi H, Yamamoto T, Okajima T, Umesaki M, Ching W Y, Inoue Y, Mizuno M, Araki H and Shirai Y 2003 *Nat. Mater.* **2** 541
[2] Rehr J J and Albers R C 2000 *Rev. Mod. Phys.* **72** 621
[3] Tanaka I, Mizoguchi T and Yamamoto T 2005 *J. Am. Ceram. Soc.* **88** 2013
[4] Mizoguchi T, Tanaka I, Yoshioka S, Kunisu M, Yamamoto T and Ching W Y 2004 *Phys. Rev.* B **70** 045103
[5] Mo S D and Ching W Y 2000 *Phys. Rev.* B **62** 7901
[6] Blaha P, Schwarz K, Madsen G, Kvasicka D and Luitz J 2001 *WIEN2k, An Augmented Plane Wave + Local Orbitals Program for Calculating Crystal Properties* Karlheinz Schwarz, Techn. Universitat Wien, Austria
[7] Monkhorst H J and Pack J D 1976 *Phys. Rev.* B **13** 5188
[8] Ohno H, Munekata H, Penny T, von Molnar S and Chang L L 1992 *Phys. Rev. Lett.* **68** 2664
[9] Ohno H, Shen A, Matsukura F, Oiwa A, Endo A, Katsumoto S and Iye Y 1996 *Appl. Phys. Lett.* **69** 363
[10] Peleckis G, Wang X L and Dou S X 2006 *Appl. Phys. Lett.* **88** 132507
[11] Jia W, Xu W, Rivera I, Perez A and Fernandez F 2003 *Solid State Commun.* **126** 153
[12] Tang J, Yu X, Yang L, Zhou C and Peng X 2006 *Mater. Lett.* **60** 326
[13] Okamoto S and Yamamoto H 2001 *Appl. Phys. Lett.* **78** 655
[14] Okajima T, Yamamoto T, Kunisu M, Yoshioka S, Tanaka I and Norimasa U 2006 *Japan. J. Appl. Phys.* **45** 7028
[15] Eguchi K, Setoguchi T, Inoue T and Arai H 1992 *Solid State Ion.* **52** 165